

Proposal of Analog In-Memory Computing with Magnified Tunnel Magnetoresistance Ratio and Universal STT-MRAM Cell

Hao Cai, *Member, IEEE*, Yanan Guo, *Student Member, IEEE*, Bo Liu, *Member, IEEE*, Mingyang Zhou, *Student Member, IEEE*, Juntong Chen, *Student Member, IEEE*, Xinning Liu, *Member, IEEE*, and Jun Yang, *Member, IEEE*

Abstract—In-memory computing (IMC) is an effectual solution for energy-efficient artificial intelligence applications. Analog IMC amortizes the power consumption of multiple sensing amplifiers with analog-to-digital converter (ADC), and simultaneously completes the calculation of multi-line data with high parallelism degree. Based on a universal one-transistor one-magnetic tunnel junction (MTJ) spin transfer torque magnetic RAM (STT-MRAM) cell, this paper demonstrates a novel tunneling magnetoresistance (TMR) ratio magnifying method to realize analog IMC. Previous concerns include low TMR ratio and analog calculation nonlinearity are addressed using device-circuit interaction. Peripheral circuits are minimally modified to enable in-memory matrix-vector multiplication. A current mirror with feedback structure is implemented to enhance analog computing linearity and calculation accuracy. The proposed design maximally supports 1024 2-bit input and 1-bit weight multiply-and-accumulate (MAC) computations simultaneously. The 2-bit input is represented by the width of the input (IN) pulses, while the 1-bit weight is stored in STT-MRAM and the $\times 7500$ magnified TMR (m-TMR) ratio is obtained by latching. The proposal is simulated using 28-nm CMOS process and MTJ compact model. The integral nonlinearity is reduced by 57.6% compared with the conventional structure. 9.47-25.4 TOPS/W is realized with 2-bit input, 1-bit weight and 4-bit output convolution neural network (CNN).

Index Terms—STT-MRAM, tunneling magnetoresistance ratio, in-memory computing, analog computing, linearity.

I. INTRODUCTION

EMerging nonvolatile memories (NVMs) accompany with better computing ways enable great potential for energy-efficient artificial intelligence applications [1]–[3]. Magnetic random access memory (MRAM) has demonstrated promising developments for in-memory computing (IMC) and near-memory computing (NMC) [4]–[6]. Compared with other resistive-type NVMs, IMC with MRAM (in-MRAM computing) shows potential with logic compatible supply voltage, relatively small variability issues and high endurance [6].

Previous in-MRAM computing realizations mainly rely on intrinsic computing ability of bit-cells [6]–[9] and circuit-level modification [10]–[13]. Circuit-level solutions e.g., Pinatubo, logic-in-memory and computing-in-memory provide Boolean

logic computation and support binary neural networks (BNN). MRAM building blocks e.g., sensing amplifier (SA) and reference cells are modified to follow the computation requirement, which could result in deteriorated memory performance.

Compared with digital IMC, analog IMC shows great merit in terms of high on-chip bandwidth and computation-area efficiency [14]. One-transistor one-magnetic tunnel junction (MTJ) 1T-1M bit-cell using spin-transfer-torque (STT) switching mechanism is with foundry supported as the most universal cell structure [15]–[17]. Unlike other nonvolatile memories, e.g., flash [18], resistive-RAM (RRAM) [19], [20] and phase change memory (PCM) [21], the analogue memory devices behavior of STT-MRAM cannot directly apply to analog computing for energy and throughput constrained applications. The main reason is that 100%-200% regular tunnel magnetoresistance (TMR) ratio is overwhelmingly difficult to fulfill the requirement of high dimensional matrix-vector multiplication (MVM). Although TMR was enhanced to 249% [22], the discrimination of anti-parallel (AP) and parallel (P) resistance is not sufficient, which can be influenced by the process variations.

In terms of circuit-level, analog IMC meets obstacles in its development due to: (1) Limited TMR causes mismatch between the impact of external input data and internal stored data on the output. (2) The analog computation behavior is more vulnerable to transistor nonlinear effects than its digital counterpart [23]. (3) Multiple bit-lines are required to enable simultaneously for cost amortization. In order to avoid inconsistency operations, processing units must fulfill the calculation requirements of different loads [24].

In order to bring in-MRAM computing into silicon realization, recent work attempt to make breakthrough through different hierarchical levels. [25], [26] integrates MTJ and Schottky diode as a rectified tunnel MR (R-TMR) device. Device fabrication indicates that it is possible to achieve more than 10000% on/off ratio can be obtained through varying DC offset. [6] applies the next-generation spin-orbit torque (SOT) MRAM to realize analog IMC at DNN interface, with R_{on} equals to 6 MOhms. A STT-MRAM prototype with NMC was demonstrated in [5]. Shift and rotate operations can be realized close to bit-cell array.

In this paper, the proposed a novel device-circuit interacted design approach, as transfer normal TMR (in MTJ device) to magnified TMR (in computation circuits). Analog in-MRAM computing is firstly implemented based on universal 1T-1M

This work is supported in part by National Key R&D Program of China under Grant 2018YFB2202800 and National Natural Science Foundation of China under Grant 61904028. (Hao Cai and Yanan Guo contributed equally to this work.)

H. Cai, Y. Guo, B. Liu, M. Zhou, J. Chen, X. Liu and J. Yang are with the National ASIC System Engineering Center, Southeast University, Nanjing 210000, China (e-mail: hao.cai@seu.edu.cn).

cell with STT switching mechanism. To realize an enlarged virtual TMR ratio for analog computing, additional peripheral circuits are implemented, including dynamic latch, current mirror with feedback, and a successive approximation (SAR) analog-to-digital converter (ADC). Nonlinear issues of analog calculation are carefully addressed. The proposal is with minimally modified peripheral circuits realization using 28-nm CMOS, and without modification of bit-cell structure.

The remainder of the paper is organized as follow: Section II explains the basic concept and reviews recent works. Section III presents proposed in-MRAM computing structure. Section IV illustrates simulation results. Finally, Section V compares the performance of this work to prior IMC schemes, and concludes this paper with future remarks.

II. PRELIMINARIES

A. Matrix Vector Multiplication

High-dimensional matrix-vector multiplication (MVM) is a dominant kernel in signal-processing and machine-learning computations [27]. Instead of accessing raw bits row by row, IMC accesses a computation result over multiple bits, thus amortizing the accessing costs. The structure of the storage array matches the computational form of MVM, so the power consumption can be amortized by implementing MVM with IMC. MVM in-memory realization can split as a combination of multiply accumulate (MAC) computations as:

$$Y_{OUT} = \sum_{i=0}^{m-1} W_i \times X_{IN,i} \quad (1)$$

where W is the weights stored in memory array, X_{IN} is the activations from external input, and Y_{OUT} is the calculation results. There are m weights and m activations involved in the MAC calculation.

MVM needs to map the parallel input data to each row, map the parallel computation to the bit cells where the data is stored, and then reduce the output data by adding up. The mapping of weights in the storage array can be represented by:

$$W = \begin{pmatrix} W_{0,n-1} & W_{0,n-2} & \cdots & W_{0,0} \\ W_{1,n-1} & W_{1,n-2} & \cdots & W_{1,0} \\ \vdots & \vdots & \ddots & \vdots \\ W_{m-1,n-1} & W_{m-1,n-2} & \cdots & W_{m-1,0} \end{pmatrix} \quad (2)$$

where n means each weight is quantified to n bits.

B. Universal 1T-1M bit-cell

Foundry-support 1T-1M bit-cell structure shows high-density and access energy efficiency in MRAM array [15]–[17]. Fig. 1(a) illustrates the basic storage element of perpendicular magnetic anisotropy (PMA) MTJ. Compared with in-plane magnetic anisotropy (IMA), PMA MTJ fulfills the thermal stability requirement, but also has no restriction of cell aspect ratio, which shows the scaling advantages of high-density integration [28], [29]. MTJ consists of two ferromagnetic electrodes (CoFeB) with a tunnel barrier layer (MgO). The top magnet is the storage layer (referred as the free layer) and the bottom magnet is the reference (referred as

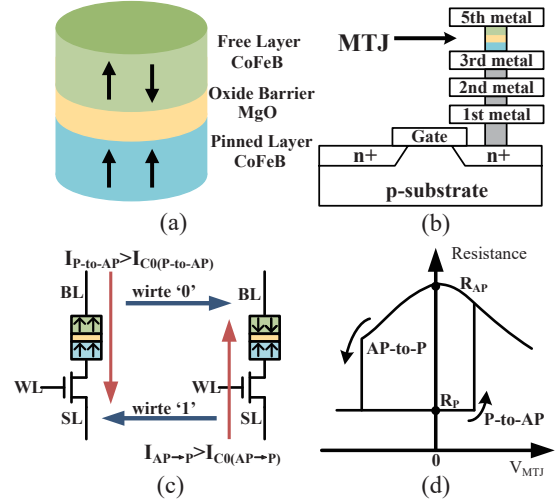


Fig. 1. (a) Sandwich structure of PMA-MTJ. (b) Cross-sectional view of 1T-1M bit-cell. (c) Universal 1T-1M bit-cell structure. (d) Resistance loop of MTJ measured by DC voltage sweep.

the pinned layer). Nonvolatile data writing is performed by injecting a spin-polarized current from one of the ferromagnetic electrodes to change the magnetic orientation of the free layer. The effective resistance of MTJ is low (R_P) when two ferromagnetic electrodes are spin aligned, and high (R_{AP}) when the magnetic direction of two layers is in the anti-parallel state. The resistance difference is represented as TMR ratio [22], [30], [31]:

$$TMR = \frac{R_{AP} - R_P}{R_P}. \quad (3)$$

Fig. 1 demonstrates the cross-sectional view, bit-cell structure and I-V characteristics of 1T-1M bit-cell. According to spin transfer torque mechanism, a bidirectional current can change the MTJ between states when it is higher than critical current I_{C0} . During the write operation, the current flowing from bit line (BL) to source line (SL) can write the data stored in MTJ as '0', while the current with opposite direction can write '1'. Fig. 1(d) shows the resistance state at different voltages and the transition of MTJ between P state and AP state.

C. Digital and analog realization of IMC

IMC is an effective way to achieve energy-efficiency emphasized non-von Neumann architecture. The principle operation of IMC is the MAC step. The few-updated weight data is stored within the memory array, and the data to be proceeded is the input from the outside. Completing part or all of the calculation in memory can reduce the power consumption caused by data transfer in the calculation. According to computation signal type and implementation approach, IMC can be classified as digital [32], [33] and analog [18]–[20], [34]–[36] computing. The framework of digital and analog IMC are illustrated in Fig. 2.

Digital IMC merges embedded memories and Boolean logic block to form processing element (PE) unit. The acceleration

TABLE I
COMPARISON OF RECENT IMC (FULL CHIP) FOR NEURAL NETWORK

	JSSC'21 [32]	ISSCC'21 [33]	JSSC'19 [34]	ISSCC'20 [35]	ISSCC'21 [36]	ISCAS'21 [18]	Nat.Com'20 [21]	ISSCC'20 [19]	ISSCC'21 [20]	ISCAS'19 [37]
Domain	Digital	Digital	Analog	Analog	Analog	Analog	Analog	Analog	Analog	Analog
Type	SRAM	SRAM	SRAM	SRAM	DRAM	Flash	PCM	RRAM	RRAM	STT-MRAM
Process	65nm	22nm	65nm	7nmFinFET	65nm	180nm	90nm	130nm	22nm	22nm
Bit-cell	6T+XNOR+MUX+FA	6T+NOR	8T+1C	8T	1T1C	1T1FTG	1PCM	2T2R	1T1R	1T-1M
Capacity	16KB×8	64Kb	36Kb×64	4Kb	16Kb	575Mb	1Mb	158.8Kb	4Mb	36Kb
Macro Area (mm ²)	1	0.202	12.6	0.0032	0.57	17.3	N/A	21.82	6	N/A
Throughput (GOPS)	6.1-567	3300 (4b/4b) 24.7 (8b/8b)	18876	372.4	4.71	29000 frame/sec ²	N/A	N/A	35.59- 417.96	N/A
Weight Bit	1-16	4/8/12/16	1	4	8(signed)	4	4	2-3(signed)	1/4/8	5
Input Bit	1-16	1-8	1	4	8	4	8	1	2/4/8	4
Output Bit	1-16	16 (4b/4b) 24 (8b/8b)	1	4	8	8	8	1-8	4/10/14	4
Computation	MAC,DNN	MAC	Binary CNN	MAC	MAC,CNN	MAC,DNN	MAC,DNN	MAC	MAC	MAC,DNN
Energy Effi. (TOPS/W)	2.06-117.3	89 (4b/4b) 24.7 (8b/8b)	866	351 ³	4.76	37 ⁴	11.9	78.4	11.91-195.7	9.7 ⁵

¹ Simulation results only without measurement data.

³ Each 4b × 4b is considered as 2 operations.

⁵ It is estimated from the data in the paper.

² The computing throughput for VGG7.

⁴ MAC only, not including other peripheral work.

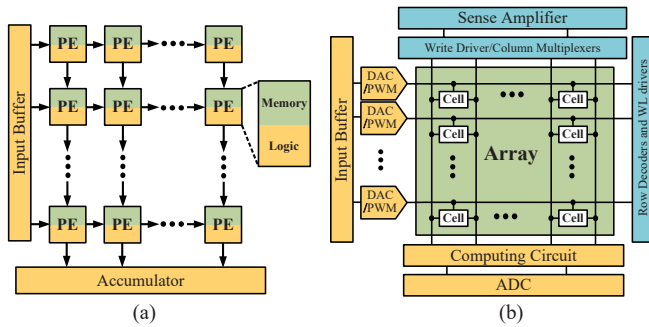


Fig. 2. Conventional IMC structure (blue blocks are read-write modules; green blocks are memory modules; orange blocks are digital or analog computing modules): (a) Digital IMC. (b) Analog IMC.

array is composed of multiple PE units. Input buffer and accumulator are responsible for data input and output, respectively.

Analog IMC retains the structure of the memory array and read-write function. External activation signals are input to each word-line (WL) through digital-to-analog converter (DAC) or pulse width modulation (PWM), and multiple rows are accessed at once. The DAC converts a digital quantity of input into a WL voltage value or the PWM adjusts the time for the high level, thus controlling the WL of each bit-cell and modulating the bit-cell current. Within the bit-cell, the weight data stored in the memory and the external input data are completed the AND operation to achieve the multiplication operation. According to Kirchhoff current law, the current flowing through each bit-cell is summarized on the bit line (BL). The result of the accumulation operation is expressed as the BL voltage drop or the voltage value on the output capacitor. Finally, an ADC converts the voltage amplitude into the digital output of memory-computation integrated block. Depending on the trade-off between precision and energy consumption, 4-8 bit ADCs are usually used in analog computing [19], [21].

Table I lists a literature study of recent IMC, including various types of memory and calculation methods. Compared with analog IMC, the digital way has the advantage of computational flexibility and accuracy. But its approach of combining logical units with bit-cells requires a lot of area overhead. The advantage of analog IMC is with high parallelism degree, which can bring enhanced throughput and energy efficiency than the digital way. Nevertheless, the design challenge of analog IMC is the design trade-off among accuracy, additional layout area and power consumption of analog components [14].

The main advantages of using static RAM (SRAM) for analog IMC are mature technology and fast computing speed. The binary logic stored in SRAM can be easily distinguished, allowing for high margins and computational linearity when multiple lines are turned on. The enhanced 8T SRMA bit-cell can effectively reduce the interference of computing to the storage data[34], [35]. [34] uses the charge sharing of capacitors to realize the addition operation, reducing the power consumption caused by the BL current and improving the energy efficiency. In [36], the columns of DRAM are configured as charge-sharing cells, and the dot product operation is accomplished by non-destructive weight reading, saving peripheral circuit area and power consumption.

NVMs, e.g., Flash, PCM and RRAM show potential for analog computing because of high resistance ratio. [19] stores multi-bit signed numbers in a 2T-2M bit-cell, and uses ADC with adjustable precision to meet different computing requirements. In [20], the multi-bit input is split and computed. Under the premise of ensuring accuracy, this method implements MAC with multi-bit I/O unit.

MRAM cannot be directly used for analog IMC due to limited TMR. [37] proposes a new analog computing structure with operational amplifier integrator circuit, which uses the difference of the current flowing through R_P and R_{AP} to complete the calculation. This method alleviates the problem of

limited TMR, but it has a high requirement on the performance of operational amplifier.

III. PROPOSAL OF ANALOG IN-MRAM COMPUTING

This section aims to solve major analog IMC design challenges: limited device TMR ratio, circuit nonlinearity and multi-bit computation configuration. The proposal refers to minimally modified memory array circuits. That is, universal bit-cell is used and the majority of MRAM peripheral circuits is retained. The dual-mode bit-cell is configured to realize magnified TMR ratio (m-TMR) for analog computing. Integrating current mirror with feedback can enhance the linearity of the analog calculation.

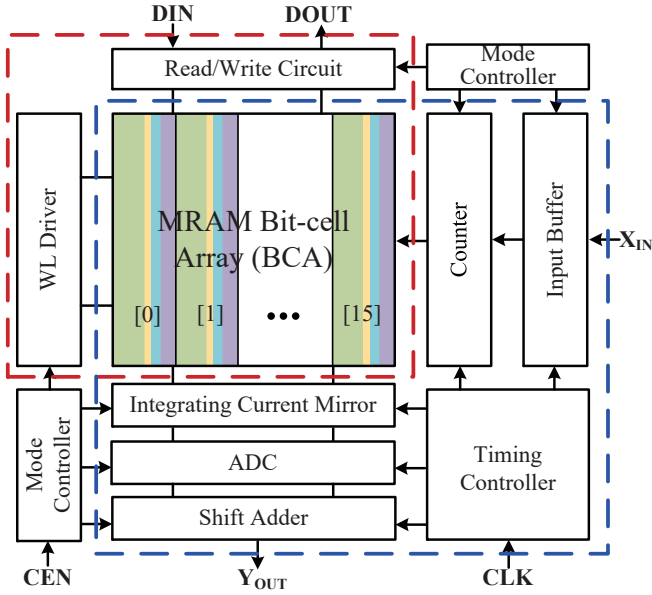


Fig. 3. Floorplan of proposed in-MRAM computing. Modified (additional) peripheral blocks mainly include: dynamic latch, current mirror with feedback and SAR-ADC.

A. The floorplan of dual-mode MRAM

Fig. 3 illustrates the block diagram of in-MRAM computing. The operation includes normal storage and IMC mode. A mode controller selects the dual-modes according to CEN (computing enable) signal. In the storage mode, the MRAM bit-cell array (BCA) executes the read-write operation as standard memory. Alternatively, computing mode is executed with analog MVM, which consists of 16 MAC operations in equation (1). As shown in Fig. 3, the MRAM BCA is divided into 16 local BCAs, each corresponding to 16 MAC operations. W is stored in the local BCA as shown in equation (2). And X_{IN} is the activations from external input, which is converted into pulse signal of corresponding width after passing the counter. The multiplication is completed in the BCA, the accumulation is completed in the integrating current mirror. Finally, Y_{OUT} is calculated using a SAR-ADC and shift adders.

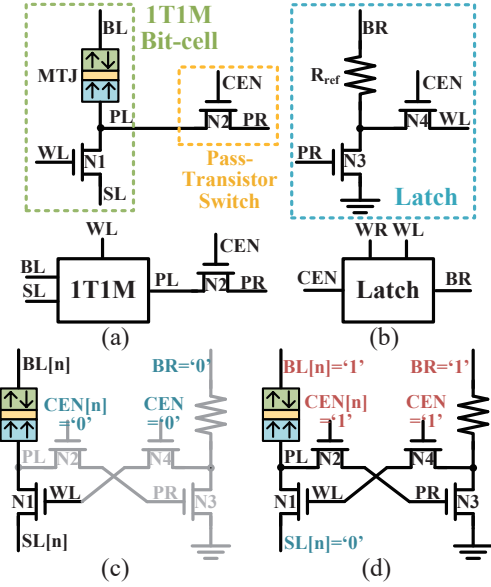


Fig. 4. (a) Structure of the 1T-1M bit-cell with a pass-transistor (PT) switch for in-MRAM computing. (b) Structure of the latch unit. (c) Normal storage mode. (d) In-MRAM computing mode.

B. The dual-mode bit-cell

As shown in Fig. 4(a), 1T-1M bit-cell is applied to normal storage mode. The pass-transistor (PT) switch N2 is allocated for in-MRAM computing mode. Compared with universal 1T-1M cell, a PT interface PL is included to initiate in-MRAM computing. The 1T-1M bit-cell structure with PT switch is regulated with BL , WL , SL , PR and CEN signals. The latch unit is consisted of two transistors and a reference resistance (R_{ref}), as shown in Fig. 4(b). The resistance value of R_{ref} is setup between R_P and R_{AP} of MTJ. This specific value is determined according to the simulation results of power consumption and latch yield, which will be elaborated in Section IV. In the local BCA, latch unit and 1T-1M cell with PT switch are connected by WL and PR . The CEN of two cells control the mode of local BCA.

Fig. 4(c) shows the working principle of the storage mode. The $CENs$ of two units are both low levels. Transistor N2 and N4 are cut-off, the proposed 1T-1M bit-cell is identical to conventional 1T-1M. It can complete read and write operations. In storage mode, W is stored in the local BCA and is the preparation for the in-MRAM computing. Compared to other storage such as SRAM, non-volatile MRAM has no static power consumption while holding data.

When $CEN[n]$, CEN , BL , BR are high and SL is low, two cross connected units are in the computing mode. As shown in Fig. 4(d), the $CENs$ of two units are both high, and two units are connected to form a latch structure. According to the resistance value of MTJ, high and low levels are generated on WL and PR to complete the latching operation. The magnetic orientation of the pinned layer is away from the transistor N1. When the resistance of MTJ is higher than R_{ref} , PR is with low level and WL is high. The MTJ is in AP state, and the magnetic orientation of the free layer is the same as the current. The high voltage difference between the two ends of

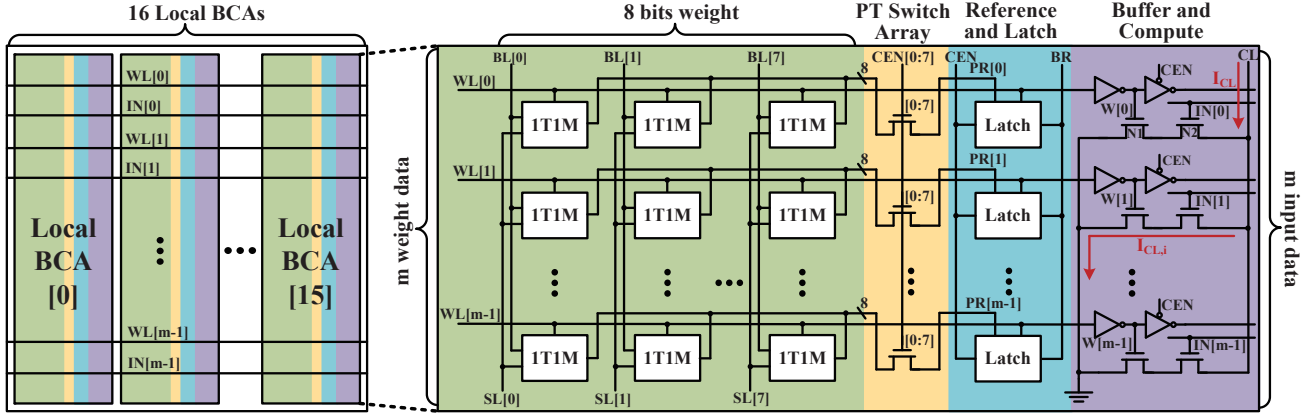


Fig. 5. The block diagram of local BCA. It mainly includes memory array using universal 1T-1M bit-cells, as well as additional PT switch array, reference-latch column and buffer-compute column in-MRAM computing.

the MTJ does not affect the data stored in the MTJ.

C. Local bit-cell array

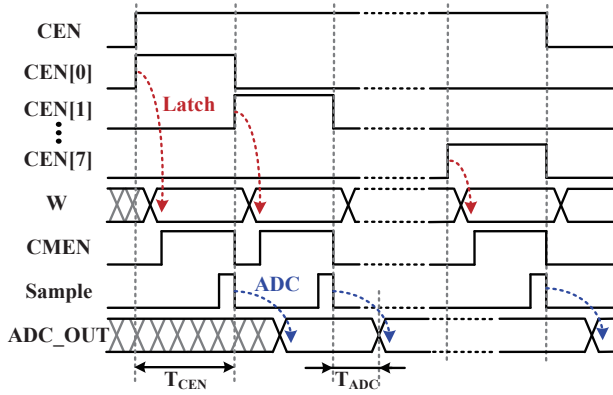


Fig. 6. Timing diagram of local BCA.

Fig. 5 shows the block diagram of local BCA, which consists of the proposed 1T-1M dual-mode cell, PT switch array, reference-latch column and buffer-compute column. The WL connect all columns in the local BCA, and the WL of 16 local BCAs are isolated by the buffer of the buffer-compute column. The PT switch array controls connection between each bit-cell and the latch unit. In the computing mode, each column of the 1T-1M bit-cell array is connected with the reference-latch column in turn to generate high and low levels on each WL using the latch structure, as shown in Fig. 6. The buffer-compute column can prevent the local BCA from interfering with each other in the computing mode. Meanwhile, the buffer-compute column can amplify the weight signal on the WL to node W using the first stage inverter of the buffer. MTJ resistance is converted into the gate voltage of transistor $N1$ by the latch structure. The TMR is ultimately amplified to the m -TMR:

$$m\text{-TMR} = \frac{R_{off} - R_{on}}{R_{on}} \quad (4)$$

where R_{on}/R_{off} is the on/off resistance of transistor.

$N1$ and $N2$ are connected in series to complete the multiplication of W and IN . IN is the input pulse generated by the activations from external X_{IN} . The voltage is provided in the computing line (CL) of buffer-compute column, and different current $I_{CL,i}$ is generated in each row, which are calculated through CL and subsequent modules. According to Kirchhoff current law, the CL current I_{CL} is given by:

$$I_{CL} = \sum_{i=0}^{m-1} I_{CL,i} \quad (5)$$

where $I_{CL,i} = I_a$ when $W[i]$ and $IN[i]$ are high, otherwise $I_{CL,i} = 0$. The computing port CL and the read-write port BL are decoupled, which can improve the computation stability and the amount of data that can be simultaneously accessed [38].

D. The associated current mirror and ADC

A local BCA corresponds to an integrating current mirror and a SAR-ADC. Fig. 6 shows the operation waveform of these modules. $CMEN$ the enabling signal of integrating current mirror. $Sample$ is the sampling signal of SAR-ADC, which overlaps with the $CMEN$ to improve the speed of in-MRAM computing. At the end of sampling, SAR-ADC converts the sampling voltage, while the array continues to calculate the next column. The operation mode of pipeline can greatly shorten the calculation delay. The calculation delay of one column is given by:

$$T = T_{CEN} + T_{ADC} \quad (6)$$

where T_{CEN} indicates the latch and compute time, and T_{ADC} is the conversion time of ADC. The more columns that are calculated, the less the average delay per column. The average delay of n columns is given by:

$$T_{AVG} = T_{CEN} + \frac{1}{n} \times T_{ADC}. \quad (7)$$

E. Operations of Input and Output

Table II lists the multiplication of 2-bit input and 1-bit weight. X_{IN} is the input via buffer, then the counter generates

a set of pulses whose width T_{IN} corresponds to the value of the activation signal. This set of pulse is connected to the IN of the buffer-compute column (see Fig. 4), and determines the calculated current conduction time for each row of the buffer-compute column. T_{CP} is the period of the CP pulse. V_a represents the output voltage corresponding to the output result of '1'.

TABLE II
MULTIPLICATION OF 2-BIT INPUT AND 1-BIT WEIGHT

MTJ	W	X_{IN}	T_{IN}	V_{OUT}
P	1	00	0	0
		01	$1 \times T_{CP}$	$1 \times V_a$
		10	$2 \times T_{CP}$	$2 \times V_a$
		11	$3 \times T_{CP}$	$3 \times V_a$
AP	0	X	X	0

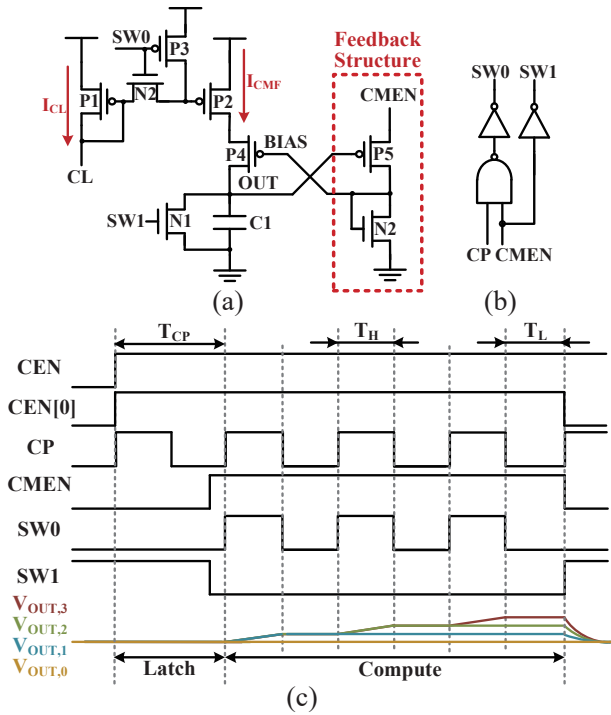


Fig. 7. (a) Circuit of integrating current mirror with feedback (CMF) structure. (b) The timing control logic circuit. (c) Waveform of computation control signals. $V_{out,1/2/3/4}$ is the output waveform of different X_{IN} .

Fig.7(a) is the circuit of integrating current mirror with feedback (CMF) structure. When reading multiple row data, the current mirror can be used to keep the read current constant, thus enhancing the calculated linearity [23]. The current I_{CL} is mirrored as I_{CMF} by the CMF structure, and the voltage of CL does not change with current charge. I_{CMF} is given by:

$$I_{CMF} = \gamma \times I_{CL} \quad (8)$$

$$\gamma = \frac{W_{P2}/L_{P2}}{W_{P1}/L_{P1}}. \quad (9)$$

Then I_{CMF} is charged to the capacitor and converted into output voltage (V_{OUT}). The charge current decreases with the increase of V_{OUT} , which reduces the linearity of the analog calculation and affects the calculation accuracy. Proposed

feedback structure of the CMF structure can reduce the bias voltage (V_{BIAS}) when V_{OUT} goes up. The charge current of the capacitor C1 is stabilized by feedback.

The timing control logic and the operation waveform of CMF structure is demonstrated in Fig. 7(b) and 7(c). SW0 controls the charging time (T_H) of each cycle, and the width of IN pulse only controls whether to charge. The SW0 of CMF structure can provide more accurate unified control of charging time than the pulse of IN . The three pulses of SW0 correspond to the 2-bit X_{IN} . $V_{OUT,i}$ is the waveform with the corresponding X_{IN} value of i for the MAC of 1 weight ($W = 1$) and 1 activation. By adjusting the number and width of SW0 pulses, CMF structure can satisfy X_{IN} of different bits. For the MAC of m weights and m activations, V_{OUT} can be represented as:

$$V_{OUT} = \sum_{i=0}^{m-1} W_i \times X_{IN,i} \times V_a \quad (10)$$

$$V_a = \frac{1}{C} \times \gamma \times I_a \times T_H \quad (11)$$

where C is the capacitance of capacitor C1.

F. SAR-ADC

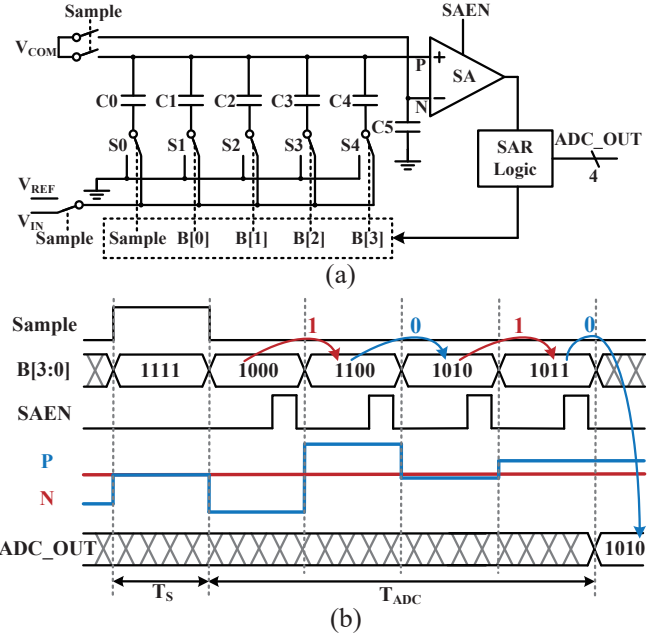


Fig. 8. (a) Schematic of 4-bit SAR-ADC. (b) Operation waveform of SAR-ADC, when ADC-OUT is '1010'.

SAR-ADC is commonly used in analog IMC because of its low cost in layout area and power consumption for multi-bits conversion. In this work, we use a 4-bit SAR-ADC as the an important peripheral circuit of the analog in-MRAM computing. Fig. 8(a) presents a schematic of the 4-bit SAR-ADC comprising five weighted capacitors (C4-C0), five switches (S4-S0), SA and SAR logic for binary search algorithm. The capacitance ratio of C4, C3, C2, C1, and C0 is 8:4:2:1:1. The top plates of the five capacitors are shorted to the node P of the SA, and the total parasitic load at node P is 16 times that of C0.

Fig. 8(b) illustrates an example of the readout operation of 4-bit SAR-ADC. At the beginning of the readout operation, the voltages at node P (V_P) and node N (V_N) are initially set to a common voltage V_{COM} ($V_P = V_N = V_{COM}$). After setting the input node to the analog input voltage V_{IN} , all five switches (S4-S0) are switched from V_{IN} to ground to decrease V_P by $(16/16) \times V_{IN}$ via ac coupling of C4-C0, such that $V_P = V_{COM} - V_{IN}$.

After the sampling is completed, it enters the conversion phase. In this phase, the SAR logic generates a control signal to switch S4 from ground to the reference voltage (V_{REF}), which supplied by the band gap reference, to increase V_P by $(8/16) \times V_{REF}$. Thus, $V_P = V_{COM} - V_{IN} + 1/2V_{REF}$. V_P is compared with V_N to determine whether V_P is higher or lower than V_N , which is essentially the comparison of V_{IN} and $1/2V_{REF}$. The output of the SA is sent to the SAR logic to determine the control of the capacitor switches in the next operation phase. When $V_P > V_N$, it means that $V_{IN} < 1/2V_{REF}$, in the next operation phase, the SAR logic generates a control signal to switch S4 from V_{REF} to ground and switch S3 from ground to V_{REF} to decrease V_P by $(4/16 - 8/16) \times V_{REF}$. Thus, $V_P = V_{COM} - V_{IN} + 1/4V_{REF}$. When $V_P > V_N$, the SAR logic generates a control signal to switch S3 from ground to V_{REF} to increase V_P by $(4/16) \times V_{REF}$. Thus, $V_P = V_{COM} - V_{IN} + 1/2V_{REF} + 1/4V_{REF}$. After 4 operation phases, the SAR logic will determine 4-bit digital code to get the final readout of the SAR-ADC.

In summary, analog in-MRAM computing was realized based on the above-mentioned proposal, using modified MRAM peripheral circuits implementation and device-circuit interaction design methods. Limited device TMR ratio can be addressed peripheral circuit within 1T-1M bit-cell based MRAM macro. The m-TMR formed by latching structure can meet the requirements of analog calculation. Circuit nonlinearity can be alleviated by the proposed CMF, which adds two additional transistors outside the current mirror. Multi-bit computing configuration allows analog computation by splitting data, converting it to a digital signal and then producing the result by a shift adder.

IV. EXPERIMENTAL RESULTS

The proposed m-TMR enlargement approach, analog in STT-MRAM computing circuits and system are verified and simulated with Spectre in Cadence Virtuoso front-end, using 28-nm CMOS process design kits and MTJ VerilogA compact model [39], [40]. The simulation conditions are typical-typical (TT) corner, 27°C, and the supply voltage (V_{dd}) is 900 mV. Table III lists fundamental MTJ parameters used in our analysis. MTJ physical parameter conforms to a commercial 40-nm critical dimension (CD) MTJ physical parameters. The effective low-resistance R_P of MTJ is 6 kΩ with spin aligned ferromagnetic electrodes. An initial 200% TMR ratio is configured.

A. Power consumption of latch structure

The reference resistance R_{ref} and the latching voltage (V_l) in latch structure affect the yield and power consumption.

TABLE III
PHYSICAL PARAMETERS OF STT-MTJ FOR IN-MRAM COMPUTING PERFORMANCE SIMULATION

Parameters	Description	Default Value
ΔH_0	Activation energy	0.8eV
Γ	Field acceleration	1.7cm/MV
β	Shape parameter	1.5
k_B	Boltzmann constant	$8.625 \cdot 10^{-5}$ eV/K
T_0	Ambient temperature	300K
Variable	Description	Default Value
t_{ox}	Oxide barrier thickness of	0.85nm
TMR(0)	TMR with 0 stress voltage	200%
Area	MTJ surface	40nm · 40nm · $\pi/4$
t_{sl}	Thickness of free layer	1.3nm
V_{sl}	Volume of free barrier	Area · t_{sl}

In order to reduce power consumption and improve latch variability performance, 5000 Monte-Carlo runs analysis is performed for R_{ref} and V_l under different TMR, and the 1-bit latch power consumption under different conditions is evaluated. Comprehensive analysis of the influence of R_{ref} and V_l on latching and selection of appropriate parameters can reduce power consumption and improve yield.

TABLE IV
SIMULATED LATCH PERFORMANCE WITH DIFFERENT TMR RATIO

TMR (%)	R_{ref} (kΩ)	V_l (mV)	Power (fJ)	Yield (%)
50	7.7	700	97.8	75.8
100	8.5	600	78.4	86.8
150	9	600	74.3	93.8
200	9.5	600	70.8	95.2
250	9.5	600	68.8	97.5

Fig. 9(a) and 9(b) show the failure probability of latch '1' and '0' under different conditions. In order to estimate the latching yield of in-MRAM computing, the voltage of the node W greater than 750 mV is '1', less than 150 mV is '0', and all other voltages are latching faults. The yield is sensitive to the change of reference resistance R_{ref} , and the latch voltage V_{latch} has different effects on the yield under different reference resistance R_{ref} . To ensure the overall yield of the latch structure, the two cases need to be considered comprehensively, and the average failure rate is shown in Fig. 9(c). When the reference resistance R_{ref} is 8.5 kΩ, 9 kΩ and 9.5 kΩ, and the supply voltage V_l is 700 mV, 700 mV and 600 mV respectively, the failure rate maintains a low level. Considering the power consumption simulation results in Fig. 9(d), the reduction of latch voltage V_{latch} has a great impact on latch power consumption. Therefore, we select reference resistance 9.5 kΩ and supply voltage V_{latch} to obtain 95.2% accuracy and 70.8 fJ power consumption. Compared with the case of 900 mV power supply voltage as V_{latch} , the result of comprehensive analysis is that the failure rate is reduced by 56.4% and the power consumption is reduced by 66.7%.

The optimal R_{ref} and V_l are obtained after trading off yield and power consumption, as summarized in Table IV. The higher the TMR, the higher the yield and the lower the power consumption. After amplification by the inverter, the m-TMR is not related to the initial TMR ratio. TMR only affects the

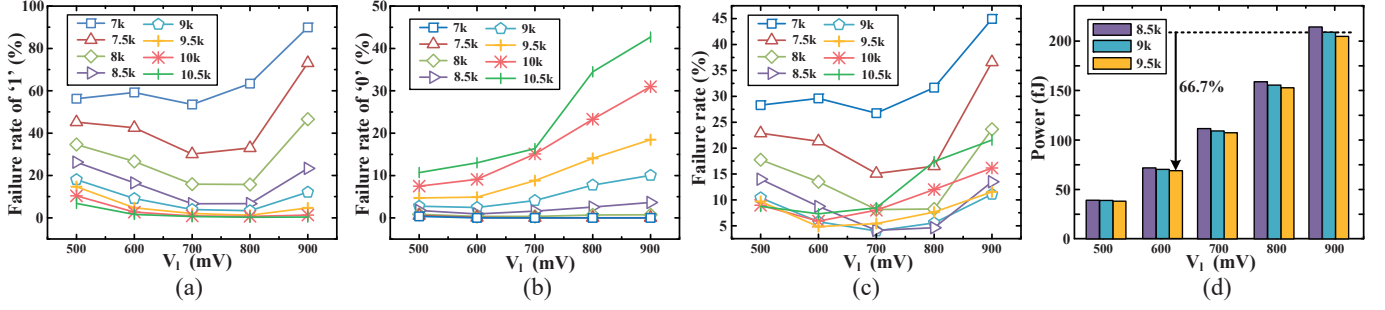


Fig. 9. Monte-Carlo simulation results of different V_I and reference resistance R_{ref} (node W voltage greater than 750mV is '1'; Less than 150mV is '0'; Other voltages are latch failure): (a) Failure rate of latch data '1'. (b) Failure rate of latch data '0'. (c) Average failure rate of latch data. (d) Latch power consumption of 1-bit weight (holding time is 4ns).

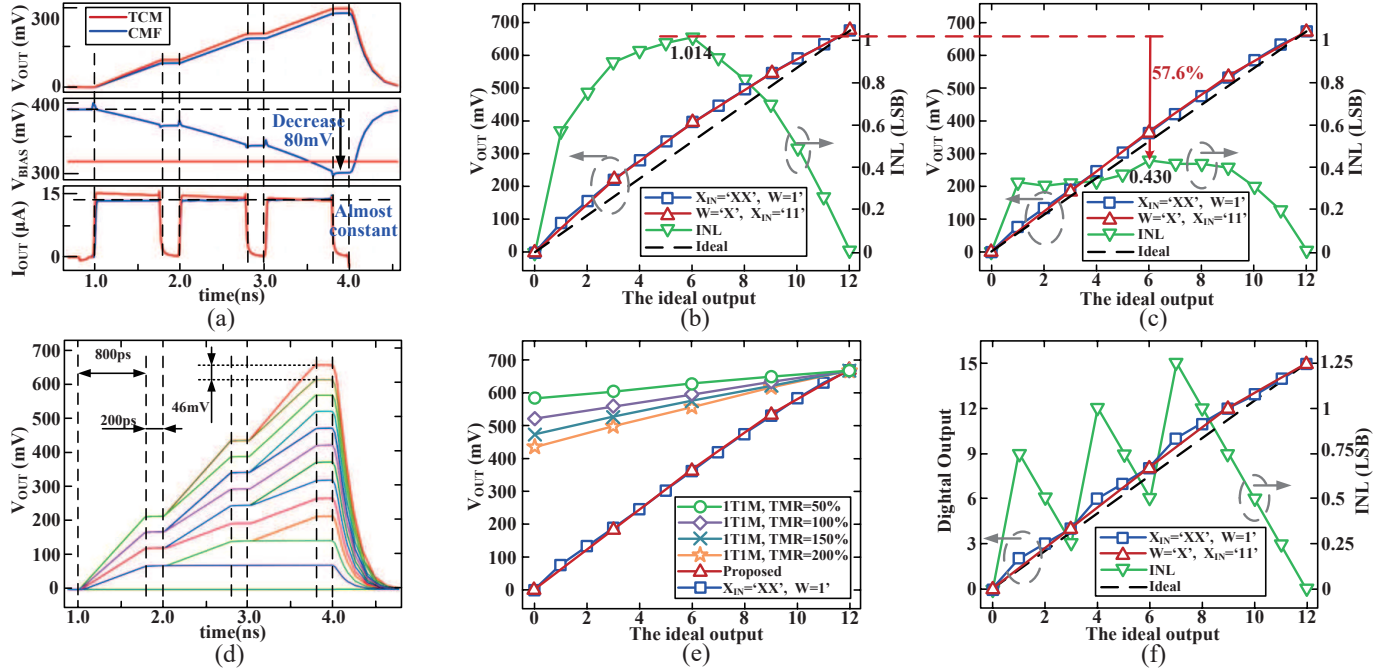


Fig. 10. (a) Operation waveform of CMF and TCM block. (b) Output voltage of TCM ('X' is 1-bit any binary number, 'XX' is 2-bit any binary number). (c) Output voltage of CMF. (d) Transient simulation results of output voltage (2bIN-1bW-4Acc, @TMR=200%). The bottom to top waveforms correspond to the calculated results from 0 to 12. (e) Output voltage of the conventional 1T-1M array and the proposed 1T-1M array under different TMR. (f) Digital output quantized by the 4-bit SAR-ADC.

yield. Simulation results show that the m-TMR is about 15000.

B. Enhanced INL

The contrast of waveforms between proposed CMF structure and traditional current mirror (TCM) is demonstrated in Fig. 10(a). V_{BIAS} of the TCM stays the same, thus the charging current I_{OUT} of the output capacitor decreases with the increase of output voltage V_{OUT} . As a comparison, V_{BIAS} of the CMF decreases 80mV with the increase of V_{OUT} , so I_{OUT} can be kept constant to enhance the linearity of the results.

Fig. 10(b) and 10(c) show the V_{OUT} versus the ideal output of TCM and CMF. Integral nonlinearity (INL) refers to the difference between the transformation curve and the ideal transformation curve along the longitudinal axis, indicating the degree to which the actual curve deviates from the ideal curve. Comparing the INL of the TCM and the CMF, it can

be found that adding feedback structure significantly improves output linearity. In Fig. 10(b), the maximum value of INL is 1.014 LSB; the maximum value of INL in Fig. 10(c) is only 0.430 LSB. The INL can be reduced by 57.6% by using a feedback structure.

The output voltage range is highly depended on the calculation margin. However, the nonlinearity of the analog calculation increases as the output voltage V_{OUT} approaches the supply voltage V_{dd} of 900 mV. The ability of the CMF structure to enhance linearity is limited. The maximum V_{OUT} should be limited to 650 mV for regular CMF operation. The maximum V_{out} can be adjusted by the voltage of the input pulse, γ of the CMF structure and the capacitance of capacitor C1.

REFERENCES

- [1] H.-S. P. Wong and S. Salahuddin, "Memory leads the way to better computing," *Nature nanotechnology*, vol. 10, no. 3, pp. 191–194, 2015.
- [2] D. Ielmini and H.-S. P. Wong, "In-memory computing with resistive switching devices," *Nature Electronics*, vol. 1, no. 6, pp. 333–343, 2018.
- [3] S. Yu and P.-Y. Chen, "Emerging memory technologies: Recent trends and prospects," *IEEE Solid-State Circuits Magazine*, vol. 8, no. 2, pp. 43–56, 2016.
- [4] M. Natsui, D. Suzuki, N. Sakimura, R. Nebashi, Y. Tsuji, A. Morioka, T. Sugibayashi, S. Miura, H. Honjo, K. Kinoshita, S. Ikeda, T. Endoh, H. Ohno, and T. Hanyu, "Nonvolatile logic-in-memory LSI using cycle-based power gating and its application to motion-vector prediction," *IEEE Journal of Solid-State Circuits*, vol. 50, no. 2, pp. 476–489, 2015.
- [5] T.-C. Chang, Y.-C. Chiu, C.-Y. Lee, J.-M. Hung, K.-T. Chang, C.-X. Xue, S.-Y. Wu, H.-Y. Kao, P. Chen, H.-Y. Huang, S.-H. Teng, and M.-F. Chang, "13.4 A 22nm 1Mb 1024b-read and near-memory-computing dual-mode STT-MRAM macro with 42.6GB/s read bandwidth for security-aware mobile devices," in *2020 IEEE International Solid-State Circuits Conference - (ISSCC)*, 2020, pp. 224–226.
- [6] J. Doevenspeck, K. Garello, B. Verhoef, R. Degraeve, S. Van Beek, D. Crotti, F. Yasin, S. Couet, G. Jayakumar, I. A. Papistas, P. Debacker, R. Lauwereins, W. Dehaene, G. S. Kar, S. Cosemans, A. Mallik, and D. Verkest, "SOT-MRAM based analog in-memory computing for DNN inference," in *2020 IEEE Symposium on VLSI Technology*, 2020, pp. 1–2.
- [7] Z. Wang, H. Zhou, M. Wang, W. Cai, D. Zhu, J.-O. Klein, and W. Zhao, "Proposal of toggle spin torques magnetic RAM for ultrafast computing," *IEEE Electron Device Letters*, vol. 40, no. 5, pp. 726–729, 2019.
- [8] J. Doevenspeck, K. Garello, S. Rao, F. Yasin, S. Couet, G. Jayakumar, A. Mallik, S. Cosemans, P. Debacker, D. Verkest, R. Lauwereins, W. Dehaene, and G. Kar, "Multi-pillar SOT-MRAM for accurate analog in-memory DNN inference," in *2021 Symposium on VLSI Technology*, 2021, pp. 1–2.
- [9] S.-h. C. Baek, K.-W. Park, D.-S. Kil, Y. Jang, J. Park, K.-J. Lee, and B.-G. Park, "Complementary logic operation based on electric-field controlled spin-orbit torques," *Nature electronics*, 2018.
- [10] S. Li, C. Xu, Q. Zou, J. Zhao, Y. Lu, and Y. Xie, "Pinatubo: A processing-in-memory architecture for bulk bitwise operations in emerging non-volatile memories," in *2016 53rd ACM/EDAC/IEEE Design Automation Conference (DAC)*, 2016, pp. 1–6.
- [11] S. Jain, A. Ranjan, K. Roy, and A. Raghunathan, "Computing in memory with spin-transfer torque magnetic RAM," *IEEE Transactions on Very Large Scale Integration (VLSI) Systems*, vol. 26, no. 3, pp. 470–483, 2018.
- [12] M. Zabihi, Z. I. Chowdhury, Z. Zhao, U. R. Karpuzcu, J.-P. Wang, and S. S. Sapatnekar, "In-memory processing on the spintronic CRAM: From hardware design to application mapping," *IEEE Transactions on Computers*, vol. 68, no. 8, pp. 1159–1173, 2019.
- [13] Y. Zhang, J. Wang, C. Lian, Y. Bai, G. Wang, Z. Zhang, Z. Zheng, L. Chen, K. Zhang, G. Sirakoulis, and Y. Zhang, "Time-domain computing in memory using spintronics for energy-efficient convolutional neural network," *IEEE Transactions on Circuits and Systems I: Regular Papers*, vol. 68, no. 3, pp. 1193–1205, 2021.
- [14] M. E. Sinangil, B. Erbagci, R. Naous, K. Akarvardar, D. Sun, W.-S. Khwa, H.-J. Liao, Y. Wang, and J. Chang, "A 7-nm compute-in-memory SRAM macro supporting multi-bit input, weight and output and achieving 351 TOPS/W and 372.4 GOPS," *IEEE Journal of Solid-State Circuits*, vol. 56, no. 1, pp. 188–198, 2021.
- [15] Y.-C. Shih, C.-F. Lee, Y.-A. Chang, P.-H. Lee, H.-J. Lin, Y.-L. Chen, C.-P. Lo, K.-F. Lin, T.-W. Chiang, Y.-J. Lee, K.-H. Shen, R. Wang, W. Wang, H. Chuang, E. Wang, Y.-D. Chih, and J. Chang, "A reflow-capable, embedded 8Mb STT-MRAM macro with 9nS read access time in 16nm FinFET logic cmos process," pp. 11.4.1–11.4.4, 2020.
- [16] G. Jan, L. Thomas, S. Le, Y.-J. Lee, H. Liu, J. Zhu, J. Iwata-Harms, S. Patel, R.-Y. Tong, V. Sundar, S. Serrano-Guisan, D. Shen, R. He, J. Haq, Z. J. Teng, V. Lam, Y. Yang, Y.-J. Wang, T. Zhong, H. Fukuzawa, and P.-K. Wang, "Demonstration of ultra-low voltage and ultra low power STT-MRAM designed for compatibility with 0x node embedded LLC applications," pp. 65–66, 2018.
- [17] V. B. Naik, K. Lee, K. Yamane, R. Chao, J. Kwon, N. Thiyagarajah, N. L. Chung, S. H. Jang, B. Behin-Aein, J. H. Lim, T. Y. Lee, W. P. Neo, H. Dixit, S. K. L. C. Goh, T. Ling, J. Hwang, D. Zeng, J. W. Ting, E. H. Toh, L. Zhang, R. Low, N. Balasankaran, L. Y. Zhang, K. W. Gan, L. Y. Hau, J. Mueller, B. Pfefferling, O. Kallensee, S. L. Tan, C. S. Seet, Y. S. You, S. T. Woo, E. Quek, S. Y. Siah, and J. Pellerin, "Manufacturable 22nm FD-SOI embedded MRAM technology for industrial-grade MCU and IOT applications," pp. 2.3.1–2.3.4, 2019.
- [18] H.-T. Lue, H.-W. Hu, T.-H. Hsu, P.-K. Hsu, K.-C. Wang, and C.-Y. Lu, "Design of computing-in-memory (CIM) with vertical split-gate flash memory for deep neural network (DNN) inference accelerator," in *2021 IEEE International Symposium on Circuits and Systems (ISCAS)*, 2021, pp. 1–4.
- [19] Q. Liu, B. Gao, P. Yao, D. Wu, J. Chen, Y. Pang, W. Zhang, Y. Liao, C.-X. Xue, W.-H. Chen, J. Tang, Y. Wang, M.-F. Chang, H. Qian, and H. Wu, "33.2 a fully integrated analog ReRAM based 78.4TOPS/W compute-in-memory chip with fully parallel MAC computing," in *2020 IEEE International Solid-State Circuits Conference - (ISSCC)*, 2020, pp. 500–502.
- [20] C.-X. Xue, J.-M. Hung, H.-Y. Kao, Y.-H. Huang, S.-P. Huang, F.-C. Chang, P. Chen, T.-W. Liu, C.-J. Jhang, C.-I. Su, W.-S. Khwa, C.-C. Lo, R.-S. Liu, C.-C. Hsieh, K.-T. Tang, Y.-D. Chih, T.-Y. J. Chang, and M.-F. Chang, "16.1 A 22nm 4Mb 8b-precision ReRAM computing-in-memory macro with 11.91 to 195.7TOPS/W for tiny AI edge devices," in *2021 IEEE International Solid-State Circuits Conference (ISSCC)*, vol. 64, 2021, pp. 245–247.
- [21] V. Joshi, M. Le Gallo, S. Haefeli, I. Boybat, S. R. Nandakumar, C. Piveteau, M. Dazzi, B. Rajendran, A. Sebastian, and E. Eleftheriou, "Accurate deep neural network inference using computational phase-change memory," *Nature communications*, vol. 11, no. 1, pp. 1–13, 2020.
- [22] M. Wang, W. Cai, K. Cao, J. Zhou, J. Wrona, S. Peng, H. Yang, J. Wei, W. Kang, Y. Zhang *et al.*, "Current-induced magnetization switching in atom-thick tungsten engineered perpendicular magnetic tunnel junctions with large tunnel magnetoresistance," *Nature communications*, vol. 9, no. 1, pp. 1–7, 2018.
- [23] Z. Lin, H. Zhan, Z. Chen, C. Peng, X. Wu, W. Lu, Q. Zhao, X. Li, and J. Chen, "Cascade current mirror to improve linearity and consistency in SRAM in-memory computing," *IEEE Journal of Solid-State Circuits*, vol. 56, no. 8, pp. 2550–2562, 2021.
- [24] C.-X. Xue, W.-H. Chen, J.-S. Liu, J.-F. Li, W.-Y. Lin, W.-E. Lin, J.-H. Wang, W.-C. Wei, T.-Y. Huang, T.-W. Chang, T.-C. Chang, H.-Y. Kao, Y.-C. Chiu, C.-Y. Lee, Y.-C. King, C.-J. Lin, R.-S. Liu, C.-C. Hsieh, K.-T. Tang, and M.-F. Chang, "Embedded 1-Mb ReRAM-based computing-in-memory macro with multibit input and weight for CNN-based AI edge processors," *IEEE Journal of Solid-State Circuits*, vol. 55, no. 1, pp. 203–215, 2020.
- [25] K. Zhang, K. Cao, Y. Zhang, Z. Huang, W. Cai, J. Wang, J. Nan, G. Wang, Z. Zheng, L. Chen, Z. Zhang, Y. Zhang, S. Yan, and W. Zhao, "Rectified tunnel magnetoresistance device with high on/off ratio for in-memory computing," *IEEE Electron Device Letters*, vol. 41, no. 6, pp. 928–931, 2020.
- [26] K. Zhang, Y. Zhang, Z. Zhang, Z. Zheng, G. Wang, Y. Zhang, Q. Liu, S. Yan, and W. Zhao, "Magnetoresistance: Large magnetoresistance and 15 boolean logic functions based on a ZnCoO film and diode combined device," *Advanced Electronic Materials*, vol. 5, no. 3, p. 1970016, 2019.
- [27] N. Verma, H. Jia, H. Valavi, Y. Tang, M. Ozatay, L.-Y. Chen, B. Zhang, and P. Deaville, "In-memory computing: Advances and prospects," *IEEE Solid-State Circuits Magazine*, vol. 11, no. 3, pp. 43–55, 2019.
- [28] H. Meng and J.-P. Wang, "Spin transfer in nanomagnetic devices with perpendicular anisotropy," *Applied physics letters*, vol. 88, no. 17, p. 172506, 2006.
- [29] N. Nishimura, T. Hirai, A. Koganei, T. Ikeda, K. Okano, Y. Sekiguchi, and Y. Osada, "Magnetic tunnel junction device with perpendicular magnetization films for high-density magnetic random access memory," *Journal of applied physics*, vol. 91, no. 8, pp. 5246–5249, 2002.
- [30] S. Yuasa, T. Nagahama, A. Fukushima, Y. Suzuki, and K. Ando, "Giant room-temperature magnetoresistance in single-crystal Fe/MgO/Fe magnetic tunnel junctions," *Nature materials*, vol. 3, no. 12, pp. 868–871, 2004.
- [31] M. Julliere, "Tunneling between ferromagnetic films," *Physics letters A*, vol. 54, no. 3, pp. 225–226, 1975.
- [32] H. Kim, T. Yoo, T. T.-H. Kim, and B. Kim, "Colonnade: A reconfigurable SRAM-based digital bit-serial compute-in-memory macro for processing neural networks," *IEEE Journal of Solid-State Circuits*, vol. 56, no. 7, pp. 2221–2233, 2021.
- [33] Y.-D. Chih, P.-H. Lee, H. Fujiwara, Y.-C. Shih, C.-F. Lee, R. Naous, Y.-L. Chen, C.-P. Lo, C.-H. Lu, H. Mori, W.-C. Zhao, D. Sun, M. E. Sinangil, Y.-H. Chen, T.-L. Chou, K. Akarvardar, H.-J. Liao, Y. Wang, M.-F. Chang, and T.-Y. J. Chang, "16.4 An 89TOPS/W and 16.3TOPS/mm² all-digital SRAM-based full-precision compute-in-memory macro in 22nm for machine-learning edge applications," in *2021 IEEE International Solid-State Circuits Conference (ISSCC)*, vol. 64, 2021, pp. 252–254.

- [34] H. Valavi, P. J. Ramadge, E. Nestler, and N. Verma, "A 64-tile 2.4-Mb in-memory-computing CNN accelerator employing charge-domain compute," *IEEE Journal of Solid-State Circuits*, vol. 54, no. 6, pp. 1789–1799, 2019.
- [35] Q. Dong, M. E. Sinangil, B. Erbagci, D. Sun, W.-S. Khwa, H.-J. Liao, Y. Wang, and J. Chang, "15.3 A 351TOPS/W and 372.4GOPS compute-in-memory SRAM macro in 7nm FinFET CMOS for machine-learning applications," in *2020 IEEE International Solid-State Circuits Conference - (ISSCC)*, 2020, pp. 242–244.
- [36] S. Xie, C. Ni, A. Sayal, P. Jain, F. Hamzaoglu, and J. P. Kulkarni, "16.2 eDRAM-CIM: Compute-in-memory design with reconfigurable embedded-dynamic-memory array realizing adaptive data converters and charge-domain computing," in *2021 IEEE International Solid-State Circuits Conference (ISSCC)*, vol. 64, 2021, pp. 248–250.
- [37] A. D. Patil, H. Hua, S. Gonugondla, M. Kang, and N. R. Shanbhag, "An MRAM-based deep in-memory architecture for deep neural networks," in *2019 IEEE International Symposium on Circuits and Systems (IS-CAS)*, 2019, pp. 1–5.
- [38] Z. Lin, Z. Zhu, H. Zhan, C. Peng, X. Wu, Y. Yao, J. Niu, and J. Chen, "Two-direction in-memory computing based on 10T SRAM with horizontal and vertical decoupled read ports," *IEEE Journal of Solid-State Circuits*, pp. 1–1, 2021.
- [39] G. Wang, Y. Zhang, J. Wang, Z. Zhang, K. Zhang, Z. Zheng, J.-O. Klein, D. Ravelosona, Y. Zhang, and W. Zhao, "Compact modeling of perpendicular-magnetic-anisotropy double-barrier magnetic tunnel junction with enhanced thermal stability recording structure," *IEEE Transactions on Electron Devices*, vol. 66, no. 5, pp. 2431–2436, 2019.
- [40] Y. Wang, H. Cai, L. A. d. B. Naviner, Y. Zhang, X. Zhao, E. Deng, J.-O. Klein, and W. Zhao, "Compact model of dielectric breakdown in spin-transfer torque magnetic tunnel junction," *IEEE Transactions on Electron Devices*, vol. 63, no. 4, pp. 1762–1767, 2016.
- [41] <https://www.eembc.org/>, "Embedded microprocessor benchmark consortium (EEMBC)," 2021.